



## Coal bottom ash derived zeolite (SSZ-13) for the sorption of synthetic anion Alizarin Red S (ARS) dye

Anjani R.K. Gollakota<sup>a</sup>, Venkata Subbaiah Munagapati<sup>b</sup>, Vikranth Volli<sup>a</sup>, Sneha Gautam<sup>c</sup>, Jet-Chau Wen<sup>a,b,\*</sup>, Chi-Min Shu<sup>a,\*\*</sup>

<sup>a</sup> Department of Safety, Health, and Environmental Engineering, National Yunlin University of Science and Technology, Douliou City 64002, Yunlin County, Taiwan, ROC

<sup>b</sup> Research Centre for Soil & Water Resources and Natural Disaster Prevention (SWAN), National Yunlin University of Science & Technology, Douliou 64002, Taiwan, ROC

<sup>c</sup> Department of Civil Engineering, Karunya Institute of Technology and Sciences, Coimbatore, Tamil Nadu 641114, India

### ARTICLE INFO

Editor: Dr. H. Artuto

#### Keywords:

Coal bottom ash  
Zeolite  
Alizarin Red S  
SSZ-13  
Adsorption

### ABSTRACT

SSZ-13 zeolite was successfully synthesized from coal bottom ash (CBA) upon hydrothermal treatment for selective sorption of Alizarin Red S (ARS) dye. The characterization of CBA, and SSZ-13 were performed using BET, SEM, FTIR, XRF, and XRD techniques. The optimal fusion ratio (CBA: NaOH) was identified as 1:3, resulting zeolite SSZ-13 with a specific surface area of 206.6 m<sup>2</sup>/g, compared to raw CBA (7.81 m<sup>2</sup>/g). The kinetics, isotherms, and thermodynamics of the ARS adsorption onto the SSZ-13, and CBA were assessed under various conditions. The results indicated that the adsorption phenomenon is optimal under acidic medium (pH = 2 for CBA, pH = 3 for SSZ-13); at ambient room temperature of 298 K; adsorbent dosage of 0.03 g, contact time of 120 min. Further, the equilibrium data fitted well to Langmuir isotherm ( $q_e = 210.75$  mg/g), following pseudo-second-order kinetics. Moreover, the chemisorption phenomenon is clearly described using Elovich kinetic model. Various thermodynamic parameters signifies the adsorption phenomenon is spontaneous, and endothermic in nature. Finally, regeneration studies revealed the sensitivity of SSZ-13 zeolite towards 0.1 M NaOH/EtOH eluent in recovery and the possibility of reuse to five successive adsorption/desorption cycles. Thus, hydrothermal treatment of CBA has potential in producing zeolites suitable to adsorption.

### 1. Introduction

Alizarin Red S (ARS) dye is a non-anionic, resilient dye listed under the category of anthraquinone, commonly used as a staining agent in the textile industry, and in biological specimens, such as invertebrate groups with mineralized bones and small invertebrate embryos (Machado et al., 2016). ARS dye is a potent oxidizing agent, chemically stable, and non-biodegradable dye, such that the preservation needs careful attention, i.e., maintaining distance from heat and moisture (Roosta et al., 2014). Also, the physical features of ARS possess higher thermal, optical and physicochemical stability (Jabeen et al., 2014) and hence improper discharge onto the water bodies can cause an unfavorable effects on marine lives, (Abbas et al., 2018; Iqbal et al., 2019; Iqbal, 2016) through the obstruction of light penetration and imminent photosynthesis.

Whereas, the repercussions of ARS on humans cause allergies, skin disorders, vision defects, and mutagenic effects (Daniel Abraham et al., 2016). Hence, handling such effluents is therefore a key environmental concern. At the same time, there is a definite need to select the appropriate pathway for the detection, separation, degradation of trace ARS compounds. In this scenario, adsorption is the quick, simple, efficient, renowned, and economical means of the removal technique when compared to the other pathways (Haroon et al., 2018). Several adsorbents were previously documented for the separation of synthetic anionic dye ARS, such as activated carbon loaded with gold nanoparticle, magnetic nanoparticles coated with polypyrrole, magnetic composites biomass of mustard husk, activated carbon, and xerogel (Fayazi et al., 2015).

On the other hand, the thriving energy demands surged the

\* Corresponding author at: Department of Safety, Health, and Environmental Engineering, National Yunlin University of Science and Technology, Douliou City 64002, Yunlin County, Taiwan, ROC.

\*\* Corresponding author.

E-mail addresses: [gollakota.iitg@gmail.com](mailto:gollakota.iitg@gmail.com) (A.R.K. Gollakota), [wenj@yuntech.edu.tw](mailto:wenj@yuntech.edu.tw) (J.-C. Wen), [shucm@yuntech.edu.tw](mailto:shucm@yuntech.edu.tw) (C.-M. Shu).

<https://doi.org/10.1016/j.jhazmat.2021.125925>

Received 2 November 2020; Received in revised form 8 March 2021; Accepted 16 April 2021

Available online 20 April 2021

0304-3894/© 2021 Elsevier B.V. All rights reserved.

utilization of coal resources, leaving behind colossal quantities of coal combustion products (CCPs). Among which coal bottom ash (CBA) is a complex anthropogenic material that is left untreated and stored in open landfills had been troublesome to, human, aquatic and groundwater contaminations upon leaching (Zhou et al., 2018). At present CBA utilization is focused mainly in road construction, embankments, construction materials, geopolymer applications etc. However, below par utilization prospects of CBA (<15%) causing massive storage, handling, and disposal concerns (Gollakota et al., 2019). Contrastingly, CBA possess abundant fractions of aluminosilicates in their composition, which are the precursors of mesoporous materials, also known as zeolites. Thus, an aligned effort to reduce the environmental pollution by the metamorphosis of CBA into zeolite would both increase the economic value and offer a sustainable approach of CBA treatment.

Recently, zeolites have progressed due to their versatile structures, designable pores, and variant applications. The conventional means of zeolites synthesis is a hydrothermal treatment involving interaction with a potent alkaline agent. Further, the type and wild of zeolite is highly influenced by critical parameters, such as solid to liquid mass ratio (S/L), reaction temperature, residence time, pressure, type of alkaline agent (NaOH/KOH) etc. (Murayama et al., 2002). Many zeolites are available on a commercial scale since decades, however, very little known about zeolite SSZ-13. Further, the synthesis of SSZ-13 zeolite is mainly from structure-directing agents, but unexplored the possibility from CBA. The typical features of SSZ-13 comprise Chabazite topology (Prodingier et al., 2016), a three-dimensional interconnected pore system with 8-membered ring windows ( $3.8 \text{ \AA} \times 3.8 \text{ \AA}$ ) and a relatively low framework density of ( $15.1\text{T}/1000 \text{ \AA}^3$ ) (Wen et al., 2015), widely used in catalysis. Besides, the hierarchical structure offers excellent mass transfer and improved accessibility of reactant molecules on the active sites without altering the shape, maintaining thermal stability and acid strength (Bing et al., 2020).

Thus, the present study exploits the possibility of synthesizing SSZ-13 zeolite from Taiwanese CBA, rather than the conventional approach of using raw coal fly ash (CFA). The secondary objective of the research is to elucidate the importance of alkali fusion ratio (CBA: NaOH), and optimizing the hydrothermal parameters in preparing zeolite frame works from CBA with enhanced physico-chemical properties. The third objective is to test the adsorption ability of anionic dyestuff ARS from the aqueous stream. Finally, a comparative analysis on the adsorption of dye via raw CBA and the zeolite SSZ-13 helps to emphasize the real need of zeolitization. This potential comparison will help to understand the impact of hydrothermal treatment, effectiveness of the adsorbent and its state of usage.

## 2. Materials and methods

The CBA used for the present study was collected from the bottom ash hopper in Taiwan Power Company in the city of Taichung, Taiwan. The standard chemicals such as sodium hydroxide (NaOH,  $\geq 97\%$ ), hydrochloric acid (HCl, 37%), sodium aluminate ( $\text{NaAlO}_2$ ), synthetic anionic dye ARS ( $\text{C}_{14}\text{H}_7\text{NaO}_7\text{S}$ , 70% dye content), ethanol ( $\text{C}_2\text{H}_5\text{OH}$ ,  $\geq 99.8\%$ ), were purchased from Sigma-Aldrich, Taiwan. All the chemicals used in the present study are of analytical grade and requires no further purification process.

### 2.1. Synthesis of zeolite

Raw CBA was finely ground and sieved with  $75 \mu\text{m}$  mesh was used in the present study for the synthesis of zeolite. Alkaline fusion method was implemented to convert the CBA into SSZ-13 zeolite. The process of alkaline fusion involves the grinding of CBA samples and mixing with the ground NaOH pellets at different mass ratios of 1:1, 1:2, 1:3 to check the best suitable ones. Later, the homogeneous mixture was then calcined in a muffle furnace at a temperature of 873 K, for 60 min, known to be the dissolution reaction (Querol, 2002). The fused product

was cooled to the ambient conditions, ground into a fine powder and transferred to the 500 mL beaker containing 100 mL of deionized water, and 20% of sodium aluminate. The addition of the sodium aluminate is to adjust the Si/Al ratio, and to increase the liquid phase concentration (Mainganye, 2012). The slurry was mechanically agitated on a magnetic stirrer at 400 rpm for 24 h, resulting in a homogenized gel. Further, the crystallization step involves the transfer of gel into 100 mL polytetrafluoroethylene (PTFE) bottles which were hermetically sealed to maintain homogenized conditions for crystallization (Gollakota et al., 2020). The crystallization temperature was held to be 393 K and the residence time of 24 h. Finally, the crystallized solution was then filtered with Whatman filter paper and then washed with deionized water for several times to obtain the neutral pH. The gel was then finally cured and aged at 423 K for 24 h to strengthen and achieve optimal morphology.

### 2.2. Characterization of adsorbent

The characterization of the adsorbent is essential to assess the physico-chemical properties. Hence, various physical, chemical characterization techniques such as X-ray fluorescence spectrometer (XRF, Bruker Si Tracer) to determine the chemical composition of the raw CBA and the zeolite SSZ-13. The crystal structure of the raw CBA and the hydrothermally treated zeolite SSZ-13 was carried out using the X-ray diffractometer (XRD, Bruker Advanced-D825A) with  $\text{Cu-K}\alpha$  radiation, operating at 40 kV and 40 mA. The XRD spectra were collected over the range of  $5^\circ$ – $60^\circ$  at a scanning rate of  $0.02^\circ$  under ambient conditions. Further, the textural properties were determined using the  $\text{N}_2$  adsorption-desorption isotherms in surface area pore size analyzer (Micrometrics, ASAP 2060). Before the analysis, the samples were degassed at  $150^\circ\text{C}$  for 12 h as a standard protocol. The specific surface area was calculated by the standard Brunauer-Emmet-Teller (BET) method. At the same time, the pore size distribution was obtained from an adsorption branch using Barrette-Joyner-Halenda (BJH) method. The surface morphology of CBA, and SSZ-13 was analyzed using the Ultra-High-Resolution Thermal Field Emission Scanning Electron Microscope (JEOL, JSM-7610F Plus) SEM analysis. The specimens were coated with a thin layer of gold using a sputter coater before scanning to make them conductive. The functional group identification was done by the Fourier transform infrared spectroscopy (FTIR, Perkin-Elmer Spectrum One) containing DTGBr detector and KBr as split beamer at a scanning range of  $400$ – $4000 \text{ cm}^{-1}$ . Finally, the adsorption studies were carried out using the UV-VIS spectrophotometer (Perkin-Elmer Lambda 850) using a quartz cell with 1.0 nm path length at the wavelength of 426 nm (Khosha et al., 2011).

## 3. Results and discussion

### 3.1. X-ray fluorescence (XRF)

Table 1 provides the chemical compositions of raw CBA, zeolite SSZ-13 with different fusion combination resultants, that are highly essential

**Table 1**  
Chemical composition of coal bottom ash and zeolite SSZ-13 (wt% dry basis).

Major oxides	Raw CBA	CBA: NaOH (1:1)	CBA: NaOH (1:2)	CBA: NaOH (1:3)
$\text{SiO}_2$	71.45	60.41	58.40	60.13
$\text{Al}_2\text{O}_3$	14.26	22.29	23.20	26.53
$\text{Fe}_2\text{O}_3$	6.66	10.40	12.58	10.11
CaO	2.30	2.49	3.14	1.43
$\text{K}_2\text{O}$	0.97	0.48	0.34	0.19
$\text{TiO}_2$	1.30	0.79	1.11	0.72
CuO	0.01	0.04	0.02	0.02
MnO	0.07	0.11	0.14	0.11
Zr	0.14	0.71	0.30	0.28
ZnO	0.01	0.02	0.01	0.07
Si/Al	5.01	2.71	2.51	2.26

for the quantification of SiO<sub>2</sub>, Al<sub>2</sub>O<sub>3</sub>. The tabular values reported significant quantities of SiO<sub>2</sub>, Al<sub>2</sub>O<sub>3</sub>, strong precursors of the zeolite synthesis. Also, the molar ratio of Si/Al drastically reduced with increasing fusion ratio when compared to the raw CBA (Table 1). The role of molar ratio (Si/Al) greatly influences the physico-chemical aspects of the zeolite, and alters the entire zeolite transformation process. It is reported by (Proding et al., 2016) that the raw material containing the molar ratio of Si/Al > 5 highly favors the synthesis of SSZ-13 zeolite, which confirms the suitability of the feedstock choice (CBA) in the present study. Apart from the other trace compositions (excluding Si, Al) namely, Fe, Ca, K, and Mg are regarded as exchangeable cations greatly influence the composition, crystal structure, and also interfere into the textural properties such as pore diameter and the surface area etc. of the product phase (zeolite). The minute trace impurities, oxides of titanium, sulfur may induce undesired secondary reactions in case of the zeolite usage as a catalyst material. Thus, the deionized (DI) water wash avoids these impurities and prevent the alteration of the material properties. After the hydrothermal treatment with different fusion ratios resulted a decrease in the Si/Al molar ratio from 5.01 to 2.26 due to the dealumination favoring the formation of SSZ-13 zeolite (Nielsen et al., 2015).

### 3.2. X-ray diffraction (XRD)

Crystallographic patterns present the mineralogy of the raw CBA and the SSZ-13 zeolite in Fig. 1(a). From the XRD patterns of the CBA, the intense spikes at  $2\theta = 16.4^\circ$ ,  $26.1^\circ$  (Kuzmickas et al., 2013),  $35.2^\circ$  (Guo et al., 2019) signifies the presence of mullite, and dominant peaks at  $21.7^\circ$ ,  $24.6^\circ$ ,  $26.57^\circ$  (Dewi et al., 2018) confirms the presence of quartz. In addition, the less intense peaks at  $29.1^\circ$  shows the traces of gypsum (Winburn et al., 2000),  $33.20^\circ$  specifies hematite (Milinovic et al., 2020), and  $40.6^\circ$  designated as kaolinite (Ward and French, 2006). The patterns are in good agreement with the XRF, confirming the presence of zeolite precursors Si, Al in CBA. Upon hydrothermal treatment, the intense peaks of CBA diffractogram were disappeared, and new peaks are visible at  $2\theta = 18.00^\circ$ ,  $23.36^\circ$ ,  $25.23^\circ$ ,  $31.02^\circ$ , and  $31.44^\circ$  (Zones, 1985) represents the formation of pure phase zeolite SSZ-13. The reason ascribed was during the alkali dissolution and hydrothermal treatment, then the structural rearrangement of CBA happens, i.e., conversion of dominant phases quartz and mullite to silicates and aluminates. Thus, the raw CBA is successfully converted into SSZ-13 zeolite, a monoclinic space group with the lattice parameters of  $a = b = 13.675$ ,  $C = 14.767$ ,  $\alpha = \beta = 90^\circ$ ,  $\gamma = 120^\circ$ , and each cell contained Si<sub>36</sub>O<sub>72</sub> (Wen et al., 2015).

### 3.3. Porous texture analysis

Table 2 presents the textural properties of the CBA, and SSZ-13 zeolite resulted from the N<sub>2</sub> adsorption isotherms at 77 K. The specific

**Table 2**

Si/Al and BET results of the CBA and the zeolite SSZ-13.

Sample	Si/Al	BET surface area (m <sup>2</sup> /g)	SA <sub>ext</sub> (m <sup>2</sup> /g)	V <sub>micro</sub> (cm <sup>3</sup> /g)	Reference
Mn/SSZ-13-1	–	223.5	–	0.14	(Ye et al., 2017)
Mn/SSZ-13-2	–	219.3	–	0.13	
Mn/SSZ-13-3	–	217.4	–	0.12	
Mn/SSZ-13-4	–	190.8	–	0.11	
Mn/SSZ-13-5	–	119.2	–	0.10	
H-SSZ-13	6	11	–	0.27	(Pham et al., 2013)
Li-SSZ-13	6	27	–	0.27	
Na-SSZ-13	6	7	–	0.24	
K-SSZ-13	6	35	–	0.18	
H-SSZ-13	12	80	–	0.29	
Li-SSZ-13	12	129	–	0.26	
Na-SSZ-13	12	123	–	0.25	
K-SSZ-13	12	121	–	0.19	
Raw CBA	5.01	7.81	4.76	0.006	This work
CBA: NaOH [1:1]	2.71	25.69	16.75	0.153	
CBA: NaOH [1:2]	2.51	74.78	4.65	0.057	
CBA: NaOH [1:3]	2.26	206.60	23.08	0.125	

surface of the CBA was reported to be 7.811 m<sup>2</sup>/g prior to hydrothermal treatment, and after the treatment forming SSZ-13 zeolite with a significant increase in specific surface area to 206.6 m<sup>2</sup>/g. The increase in the surface area corresponds to the surface roughness and the generation of cracks due to the action of alkali agent NaOH on CBA dispersion and dissolution. Moreover, the alkali agents tend to swell the matrix, exerts pressure on the pore walls resulting dilations, thereby creating additional vacant sites in the matrix (Adeyemo et al., 2017). Also, the hydrothermal treatment leads to open up the extended entrapment of N<sub>2</sub> molecules altering the values of Si/Al, enhancing the surface area of the zeolite SSZ-13, and similar cases were reported to the zeolites, zeolite-X (Widiastuti et al., 2014). The adsorption/desorption isotherm of CBA (Fig. 1b) resembles Type H2 hysteresis is a resultant of wide distribution of independent pores with the narrow size distribution of main cavities, thus pore blocking/percolation holds the key in lowering specific surface area. On the other hand, Type H4 Hysteresis was reported to SSZ-13 zeolite (Fig. 1c), due to the capillary condensation within the relative pressure of  $0.1 < P/P_0 > 0.65$  indicating the interconnection of pores, which do not regulate the evaporation of adsorbed nitrogen (Thommes et al., 2015). Moreover, the pore size distribution plot Fig. 1(b), and 1(c) presents the relation among the pore volume and pore diameter of CBA with pore volume of 0.006 cm<sup>3</sup>/g, and similar values were reported by Patrick et al. (2017). Whereas, zeolite SSZ-13 resembles cage like pore

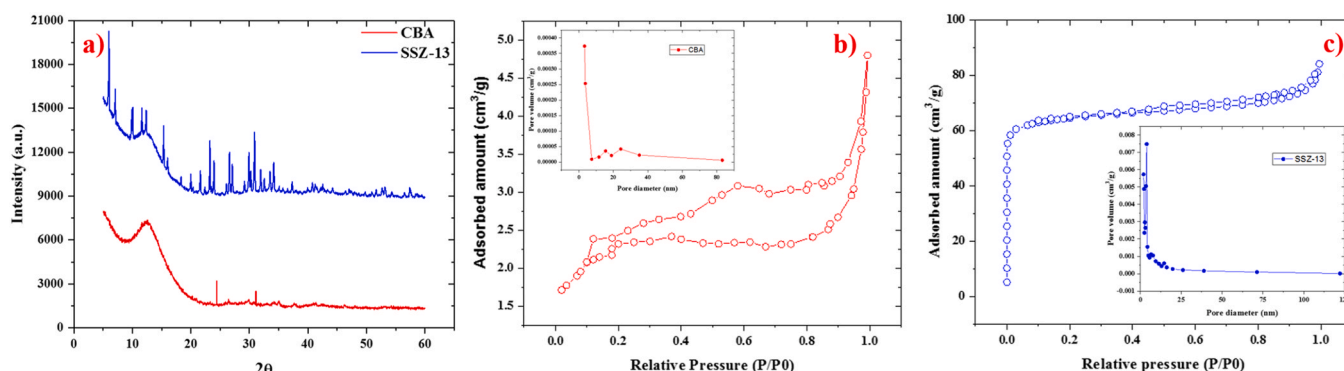


Fig. 1. (a) XRD, (b, c) N<sub>2</sub> adsorption-desorption isotherms, BJH pore size distribution images of CBA, and SSZ-13.

structure with improving pore volume of  $0.125 \text{ cm}^3/\text{g}$  due to the hydrothermal treatment and similar instances were reported by Li et al. (2016).

### 3.4. FTIR analysis

Fourier transform infrared (FTIR) spectrometer provides detailed information on the functional groups present in the selected components, i.e., CBA, and SSZ-13 in the current scenario. Information of functional groups helps to evaluate the possible attachment of sorbate on the surface of the sorbents (Belskaya et al., 2012). The FTIR spectra of the sorbent obtained in the scanning range of  $400 - 4000 \text{ cm}^{-1}$  and the bands were presented in three different figures Fig. 2(a–d) for a clear vision and better understanding of peaks at respective frequencies. For both the CBA, and SSZ-13 zeolite, the intensity of the peaks and changes are rapid in the range of  $400 - 800 \text{ cm}^{-1}$ , after that there are subtle variations visible. From Fig. 2(a–d) the FTIR spectra of CBA presents the spectrum range of  $400 - 1100 \text{ cm}^{-1}$  denotes the presence of minerals, such as quartz, kaolinite, illite, and montmorillonite etc. From this, the presence of quartz was confirmed by the intense peaks at  $465 \text{ cm}^{-1}$ ,  $509 \text{ cm}^{-1}$ , and  $550 \text{ cm}^{-1}$  (Yin et al., 2019), kaolinite peak at  $431 \text{ cm}^{-1}$  (Yin et al., 2019), traces of anhydrite at  $614 \text{ cm}^{-1}$  (Yin et al., 2019), feldspar  $645 \text{ cm}^{-1}$  (Yin et al., 2019), and Muscovite at  $1062 \text{ cm}^{-1}$  (Yin et al., 2019) respectively. Further peaks at  $2343 \text{ cm}^{-1}$  denotes O-H stretching (Katara, 2014),  $2934 \text{ cm}^{-1}$  indicating C-H stretching vibrations (Li et al., 2014), and  $2853 \text{ cm}^{-1}$  denotes the presence of organic carbon (Song et al., 2001), respectively.

On the other hand, the FTIR spectrum of SSZ-13 shows the disappearance of intense CBA bands, while enabling a new set of peaks conferring the zeolite formation. A known fact of asymmetric stretching is predominant for zeolites in the range of  $950 - 1250 \text{ cm}^{-1}$  (Breck, 1974). Further, the spectrum range of  $500 - 650 \text{ cm}^{-1}$  is prominent to for Al-O-Si stretching vibrations of amorphous contributions (Hartmann et al., 2012). As mentioned earlier the intense peaks of  $453$ ,  $463$ ,  $479$ , and  $490 \text{ cm}^{-1}$  denotes the T-O bending vibrations of  $\text{SiO}_4$  (Ghasemi and Younesi, 2012),  $\text{AlO}_4$  internal tetrahedral (Ferone et al., 2005), internal bending modes of Si-O-Al, T-O (Neville, 2016), and O-T-O bending (Bärtsch et al., 1994) vibrations respectively. Further, Symmetric stretching of Si-O-Si is witnessed at  $730 \text{ cm}^{-1}$  (Somderam et al., 2019),  $\text{N}_2$  stretching mode at  $2333 \text{ cm}^{-1}$  (Geobaldo et al., 2003), C-H band stretch at  $2927 \text{ cm}^{-1}$ ,  $2852 \text{ cm}^{-1}$  (Włodarski et al., 2020). Finally, the presence of the OH groups and the hydroxyl groups bridged to Al-OH-Si were shown at peaks  $3616$ , and  $3738 \text{ cm}^{-1}$  (Datka and Tuznik, 1985), respectively. Thus, the FTIR spectrum confers the structural rearrangement of CBA due to hydrothermal treatment tends to form zeolite SSZ-13.

### 3.5. Morphological observations

Scanning electron microscopy (SEM) determines the size distribution and the morphology of the adsorbents (CBA, and SSZ-13). Fig. 3(a, b) shows the SEM micrograph of the raw CBA, which are perfectly

spherical, glassy smooth before the hydrothermal treatment. The presence of spherical particles confirms the higher proportions of Si and Al, precursors to zeolite synthesis (Argiz et al., 2017). Fig. 3(c) presents the morphological structure of the hydrothermally synthesized zeolite material of fusion ratio (CBA: NaOH) 1:1. From the Fig. 3(c), there is no specific shape of the zeolite crystal formation observed, and the mostly residual template is visible. The reason ascribed for no particular shape of the crystal formation is due to an insufficient quantity of alkali agent (NaOH). Further Fig. 3(d) shows an improved cubical crystal structure formation (Bruzzese et al., 2020) for the fusion combination of 1:2 (CBA: NaOH). However, no confirmation yet on specific type of zeolite, i.e., mixture phase zeolite phase was confirmed and the preliminary validation of forming SSZ-13 zeolite. Further increasing the ratio of CBA: NaOH to 1:3, pure phase SSZ-13 zeolite crystals are visible all over with no other shapes were identified, confirming the pure form of the zeolite and can be seen in Fig. 3(e, f). Hence, the optimized fusion ratio of 1:3 had been chosen to the present study and zeolite (SSZ-13) obtained at this ratio has been considered in the subsequent analyses. From this, it is evident that the fusion ratio (CBA: NaOH) plays a crucial role in defining the shape, structure and the homogeneity of the zeolite. The role of NaOH at higher temperatures forces the dissolution of Si and Al, and the subsequent hydrothermal treatment paces the nucleation (Bieseki et al., 2013), crystal growth (Nishi and Thompson, 2002), and the phase transition, i.e., the internal change of energy of crystal structure (Barrer, 2007). Thus, the crystallization step and the phase transition step were two vital aspects upon which the crystal structure formation and arrangement is dependent on (cubical arrangement) (Wang et al., 2020) in the present scenario. Further, SSZ-13 has classified under Chabazite (CHA) topology consisting of an eight-member ring structure with alternate  $\text{SiO}_4$ , and  $\text{AlO}_4$  tetrahedrons interconnected with oxygen bridges and considered as micropore zeolite (Wang et al., 2010). This distinctive eight-membered structure enabling the excellent thermal stability possessing large surface area, and hence can be used as an adsorbent and as a catalytic agent (Mandal et al., 2020).

### 3.6. Adsorption experiments

The adsorption of the ARS dye on raw CBA, and hydrothermally treated CBA was investigated in batch mode sorption equilibrium experiments. All batch experiments were carried out in 100 mL glass-stoppered, Erlenmeyer's flasks containing fixed amount of the adsorbent (0.03 g) with 30 mL dye solution of known initial concentration. The flasks were tightly sealed and agitated at a constant speed of 200 rpm for 120 min in an incubator shaker maintaining optimal temperature of  $T = 298 \text{ K}$ . The influence of pH (2–10), contact time (0–300 min), dosage (0.03 - 0.1 g)/30 ml initial dye concentration of (100–1000 mg/L), and the temperature (298, 308, 318, and 328 K) were evaluated during the present study. The samples were collected from the flasks at predetermined time intervals for analyzing the residual dye concentration in the solution. The residual amount of dye in each flask was investigated using UV-VIS spectrophotometer. The amount of dye adsorbed per unit adsorbent (mg dye per g adsorbent) was calculated

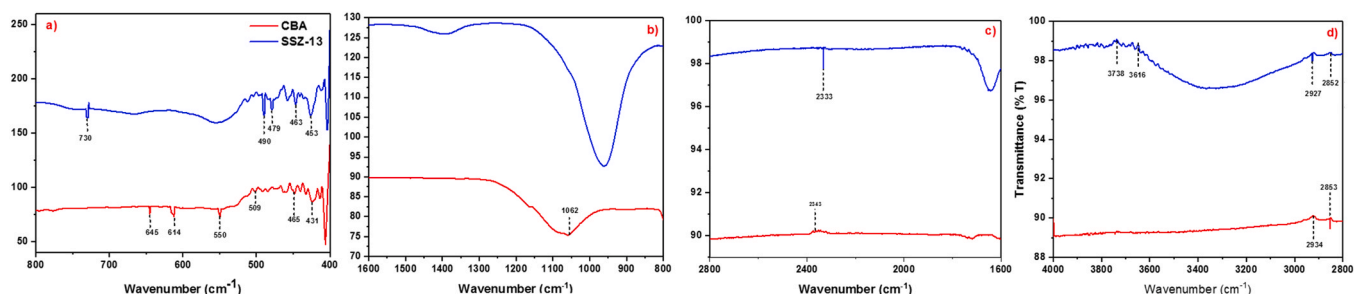


Fig. 2. (a–d) FTIR Spectrum of CBA, and SSZ-13.

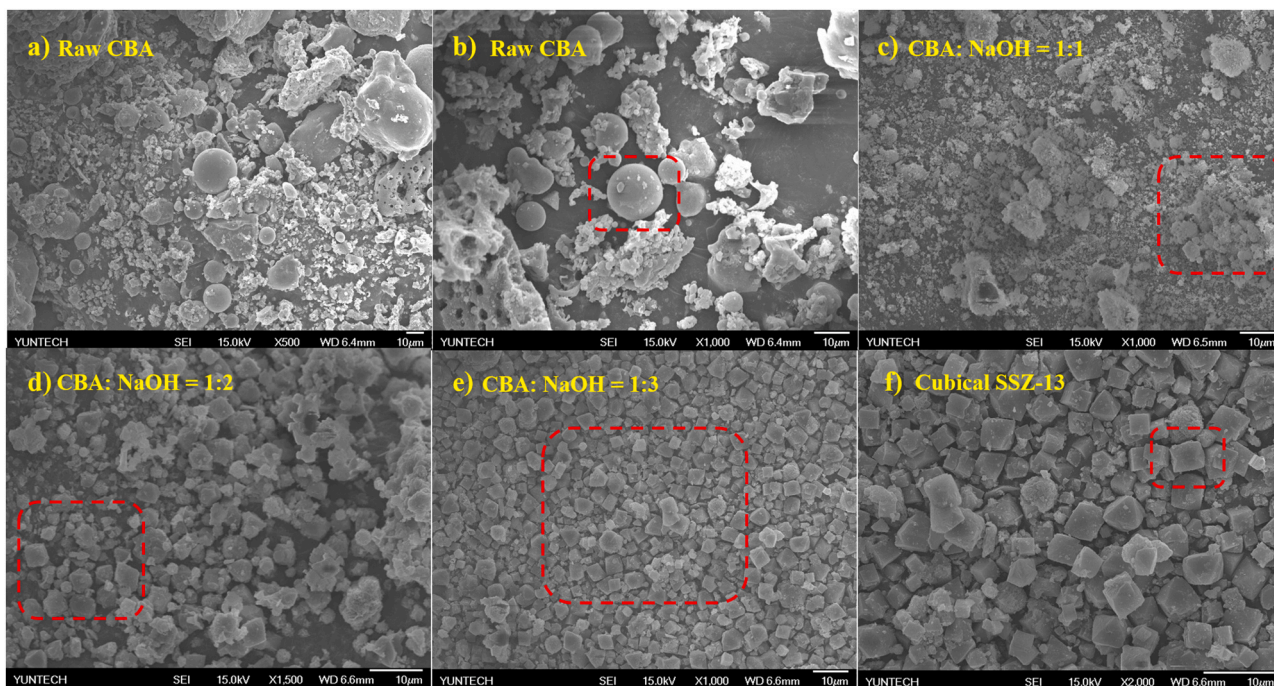


Fig. 3. (a, b) SEM micrographs of CBA, (c, d, e) zeolite formation at variable fusion ratio, (f) cubical crystal structure of SSZ-13.

according to the mass balance on the dye concentration Eq. (1), and the percentage desorption can be estimated by using Eq. (2).

$$q_e = \frac{(C_i - C_e) V}{m} \tag{1}$$

$$\text{Desorption (\%)} = \frac{\text{Desorption}}{\text{Adsorption}} \times 100 \tag{2}$$

where  $C_i$  is the initial dye concentration (mg/L),  $C_e$  is the equilibrium

dye concentration in the solution (mg/L),  $V$  is the volume of the solution L,  $m$  is the weight of the CBA, and zeolite SSZ-13 in g. All the experiments were performed triplicate and the average value from results were taken. In an adsorption study, it is necessary to fit the equilibrium adsorption data using different isotherm models, and kinetic equations to design an optimal adsorption process.

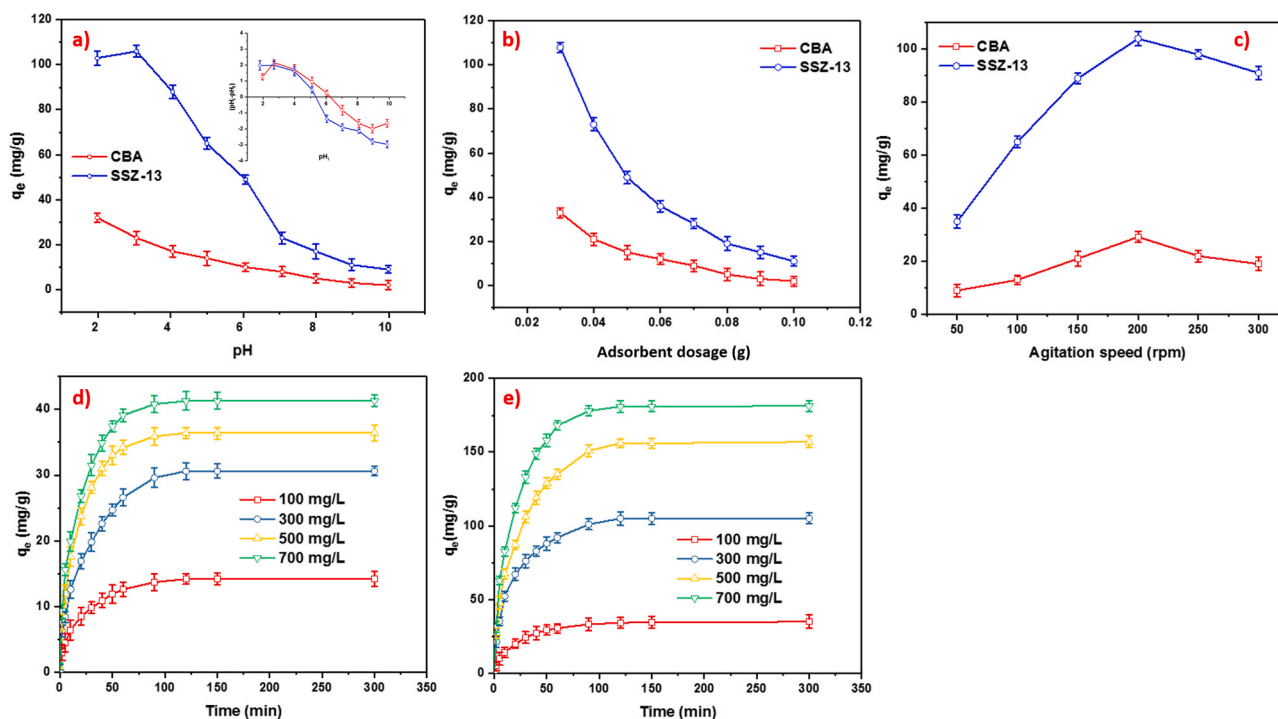


Fig. 4. Effect of process parameters on adsorption capacity (a) pH, pzc (inset), (b) dosage, (c) agitation speed, (d) effect of time using CBA adsorbent, (e) effect of time using SSZ-13 adsorbent.

### 3.7. Effect of pH

The effect of pH on the sorption of ARS dye using CBA and SSZ-13 has been investigated. Solution pH is a master variable, and inevitable in the adsorption process, as it greatly influences the adsorption capacity of the dye on to the adsorbate surface. Besides, solution pH has a direct impact on both adsorbent and adsorbate, i.e., the surface charge varied significantly with pH in case of the adsorbent. In contrast, the degree of ionization (Haghseresht et al., 2002), dissociation of the functional groups on the active sites (Madrakian et al., 2011), and the chemical structure of the adsorbate are dependent on the pH. In this study, the influence of pH has been studied in the range of (2–10) under the optimal conditions of 0.03 g adsorbent dosage, the contact time of 120 min, maintaining ambient room temperature of 298 K. The solution pH has been adjusted to the acidic environment by adding 0.1 N HCl, the alkaline conditions are maintained with the 0.1 N NaOH solution. From the Fig. 4(a), the maximum uptake capacity of the dye was spotted at pH = 2 with the sorbent CBA, while it is maximum at pH = 3 for SSZ-13. The declining patterns of pH were observed in both the case of raw CBA and SSZ-13, ascribes the reduction in vacant adsorption sites on the sorbent molecule. In addition, the higher adsorption tendency at low pH may be due to increased protonation and neutralization of the adsorbents' opposing surface charges, promoting the process of diffusion. Contrastingly, pH increases, i.e., deprotonation occurs going towards the alkaline medium, preventing the dye molecule from spreading to the adsorbent surface (Mittala and Gupta, 2010). Thus, acidic conditions are highly favorable for both the adsorbents (CBA, and SSZ-13) to adsorb the anionic dye molecules when compared to the alkaline medium.

### 3.8. Point of zero charge with effect of $pH_{pzc}$

Based on the point of zero charge ( $pH_{pzc}$ ) on the adsorbent surface, the exact process of adsorption and pH confirmation can be evaluated. The mechanism is exceptionally well established and reported by (Benhouria et al., 2015), and the same has been implemented in the present study. Briefly, explaining the procedure, the initial pH of the aqueous solution (0.01 M NaCl) was adjusted in the pH range of 2–10 using 0.1 N HCl, or 0.1 N NaOH. It is known that the cationic adsorption is more significant in the case of  $pH \geq pH_{pzc}$ , while the anionic adsorption dominates in the case of  $pH \leq pH_{pzc}$  (Gomri et al., 2018). Fig. 4(a) depicts the zero point charge of the raw CBA and the SSZ-13 were reported to be 6.25, and 5.32 signifies the negatively charged cationic adsorbent surface (CBA, and SSZ-13) readily accepts the anionic dye ARS and vice versa. Thus, the present research reported  $pH < pH_{pzc}$  signifying the anionic adsorption, i.e., ARS dye on to the CBA, and SSZ-13.

### 3.9. Effect of adsorbent dosage

The overall economy of the adsorption relies on the dosage of the adsorbent, i.e., excessive consumption of the adsorbent for the separation increase processing cost. Hence, the adsorption dosage has been optimized by considering eight dosages in the range of (0.03 - 0.1 g)/30 ml, maintaining pH = 2 in the case of the CBA, and pH = 3 for SSZ-13 at 298 K. Fig. 4(b) shows the effect of adsorption dosage of CBA, and SSZ-13 on the adsorption of ARS dye. It is observed that the dye uptake capacity decreased from 33 to 2 mg/g for CBA and, 108–11 mg/g for SSZ-13. As the dosage increased, the concentration gradient among the dye molecules and the adsorbent increases leads to the aggregation causing a lesser amount of dye transfer per unit mass onto the adsorbent (Metin et al., 2013). Another fact of this declining trend is a result of adsorbent active pore site blockage or attaining the saturated state that confined the sorption of the dye molecule (Pourjavadi et al., 2015). Thus, the present study confirms the minimal dosage of 0.03 g/ 30 mL was highly suitable for the dye uptake in the case of both CBA and SSZ-13.

### 3.10. Effect of agitation speed

During the adsorption, the transfer rate of the solution particle is greatly affected by the thickness of the liquid film covering the particle, a sole resultant of agitation speed. Besides, agitation is as important as others, ensuing proper mixing of solute and solvent that assists in forming the boundary layer, thereby promoting the film transfer coefficient (Shiau and Pan, 2004). In the present study, a series of adsorption experiments were performed by varying the agitation speeds in the range between 50 and 350 rpm, maintaining pH = 2 for CBA, pH = 3 for SSZ-13, at 298 K. The adsorption capacity concerning the variable agitation speed and with the parameters mentioned above are shown in Fig. 4(c). From the Fig. 4(c) it is understood that the adsorption of dye is optimal at 200 rpm, i.e., 29.05 mg/g for CBA, 104.12 mg/g in the case of SSZ-13, and after that decreases for both adsorbents CBA, and SSZ-13. The reason ascribed for such a phenomenon indicating the film thickness has an insignificant effect when the agitation rate is beyond 200 rpm. Another factor for the declining trend of at higher rpm is mainly due to the detachment of the dye molecules from the surface of the adsorbent experiencing centrifugal force (Chowdhury et al., 2011). Thus, 200 rpm has been found optimal in the present scenario and has been maintained throughout the study.

### 3.11. Effect of contact time and initial ARS dye concentrations

A series of contact time experiments have been performed to test the adsorption of ARS dye on the surface of CBA and SSZ-13 adsorbents at variable dye concentrations of 100, 300, 500, and 700 mg/L, maintaining pH = 2 for CBA, pH = 3 for SSZ-13, and temperature 298 K. The effect of contact time on ARS dye removal at different initial concentrations (100-700 mg/L) onto CBA, and SSZ-13 is shown in the Fig. 4(d, e). At the initial stages, the saturation curve increases steadily, suggesting the abundance of the active sites and readily accessible. The result also shows that the maximum dye adsorption using CBA reaches 41.4 mg/g at 700 mg/L Fig. 4(d), whereas it is 180.92 mg/g at 700 mg/L Fig. 4(e) in the case of SSZ-13, at the optimal contact time of 120 min which is a four-fold increase. After 120 min, the adsorption rate has been decreased, which leads to a plateau, indicating the saturation point of the adsorbent (Shigemoto et al., 1993). Moreover, the reason for such a phenomenon is that most vacant sites are available for adsorption during the initial stage and the remaining vacant sites are hard to utilize due to the existence of repulsive forces of dye molecule present on the surface of the adsorbent and the bulk phase (Karthick et al., 2018). Another relevant finding is that the rise in the initial dye concentration improved the potential of adsorption. The increased uptake capacity is attributed to the boundary layer effect, i.e., the time of dye molecule diffusion from the boundary layer to the adsorbent surface (Blackburn, 2004) and the porous structure of CBA, and SSZ-13 adsorbents. Further, the initial concentration of ARS dye provided the driving force to surpass the resistance of mass transfer between the aqueous and solid phase.

### 3.12. Isotherm studies

The study of adsorption isotherms is extremely crucial, as it provides the detail surface properties of the sorbent, adsorption behavior and the design of the adsorption system. As known, the adsorption equilibrium is a dynamic phenomenon achieved through the rate of adsorption equal to the rate of desorption. The experimental equilibrium data of ARS dye adsorption onto the CBA, and SSZ-13 adsorbents maintaining pH = 2 (CBA), pH = 3 (SSZ-13), and 298 K were fitted to the Langmuir and Freundlich isotherm models shown in Fig. 5(a, b), and the relevant equations are as follows Eqs. (3 and 4):

$$\text{Langmuir isotherm model : } q_e = \frac{q_m K_L C_e}{1 + K_L C_e} \quad (3)$$

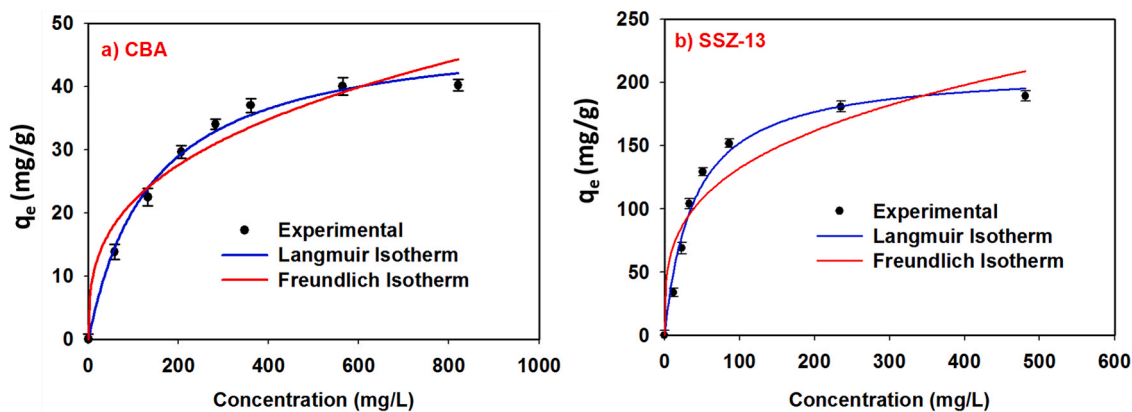


Fig. 5. Nonlinear adsorption isotherm studies varied with dye concentration (a) CBA, (b) SSZ-13.

$$\text{Freundlich isotherm model : } q_e = K_f C_e^{1/n} \quad (4)$$

where  $q_e$  (mg/g) and  $C_e$  (mg/L) are the adsorption capacity and the adsorbate equilibrium concentration in solution respectively;  $q_m$  (mg/g) is the maximum adsorption capacity;  $K_L$  (L/mg) is a adsorption energy dependent constant;  $K_f$ ,  $n$  are the Freundlich adsorption capacity and intensity measurement constants.

### 3.13. Freundlich isotherm model

The aim of the model is mainly to study the heterogeneous systems and deals with the multilayer adsorption phenomenon (Freundlich, 1907). The prime indicator  $K_f$  (Freundlich adsorption capacity) decides the feasibility of the adsorption, and in the present case, the value of  $K_f$  is 4.655 mg/g for CBA, 34.39 mg/g for SSZ-13. Similarly, adsorption intensity  $n$  is a measure of adsorptions model. In detail, if  $n > 1$  highly favors adsorption,  $n < 1$  is least preferred, and  $n = 1$  probes linear adsorption. Further, the calculated Langmuir and the Freundlich isotherm parameters are summarized in Table 3. Also, the value of  $R^2$  obtained from the plot (0.9554 for CBA, 0.9005 for SSZ-13) presenting a good fitness of this model for sorption studies Fig. 5(a, b).

### 3.14. Langmuir isotherm model

Contrasting to the Freundlich isotherm, Langmuir isotherms are designed to evaluate the monolayer adsorption phenomenon (Armbruster and Austin, 1938). Similar, to the Freundlich model, the fitness factor of the model was dependent on the dimensionless constant  $K_L$ . In case of  $K_L$  falling in between 0 and 1, is considered as the appropriate for the adsorption mechanism, and in the present study the values of  $K_L$  falls within the limit, i.e., 0.0071 L/mg for CBA, 0.0258 L/mg for SSZ-13 satisfied the feasibility criterion. In addition, the ARS dye experimental equilibrium data was compared with the theoretical equilibrium data from the Langmuir isotherm model shown in the Fig. 5(a, b). It can be seen from the figure that the isotherm plots for ARS adsorption and the calculated parameters showed that the Langmuir isotherm model fitted well with high  $R^2$  value indicating the monolayer adsorption phenomenon. Besides, the value of  $n > 1$  signifies

that the adsorption of ARS onto the CBA, and SSZ-13 is highly favorable. The full potential of adsorption for ARS is observed to be 210.75 mg/g for SSZ-13 and 49.26 mg/g for CBA. Likewise, various adsorption parameters such as correlation coefficient  $R^2$ ,  $K_f$ ,  $K_L$ ,  $n$ ,  $q_m$ , values are presented in Table 3.

Besides, the adsorption studies at lower concentration ranges between 10 and 100 mg/L were performed, yielded a very low adsorption capacity of 15.25 mg/g for CBA and 25.69 mg/g for SSZ-13 zeolite. The relevant results and the values of variables are presented in Table 3, respective plots in Fig. S1. Hence, we have performed the adsorption studies at the higher dye concentration levels in the range between 100 and 1000 mg/L.

Thus, evaluating both Freundlich and Langmuir isotherms, the present study falls under the category of the monolayer adsorption following Langmuir isotherm in comparison to the Freundlich isotherm fit. Further, the summary of literature pertaining ARS adsorption using various adsorbents is presented in Table 4.

### 3.15. Adsorption kinetics

In explaining the solute uptake rate and residence time required for the adsorption phenomenon, kinetics are of prime importance. The time dependence of the ARS dye adsorption on to CBA, and SSZ-13 was further studied with famous pseudo-first-order (Lagergren, 1989), pseudo-second-order (Ho and McKay, 1999), and Elovich (Austin Taylor and Thon, 1952) kinetic models respectively. The linear and non-linear forms of the equations are as follows Eqs. (5–10):

$$\text{Linear Pseudo – first order : } \log(q_e - q_t) = \log(q_e) - \frac{k_1}{2.303} t \quad (5)$$

$$\text{Linear Pseudo – second order : } \frac{t}{q_t} = \left( \frac{1}{k_2 q_e^2} \right) + \left( \frac{1}{q_e} \right) t \quad (6)$$

$$\text{Linear Elovich } q_e = \left( \frac{1}{\beta} \right) \ln(\alpha\beta) + \left( \frac{1}{\beta} \right) \ln t \quad (7)$$

$$\text{Nonlinear Pseudo – first – order : } q_t = q_{e1} (1 - \exp(-k_1 t)) \quad (8)$$

Table 3  
Equilibrium modeling data for the removal of ARS using CBA, and SSZ-13.

Adsorbent	Langmuir					Freundlich			
	$C_e$ (mg/L)	$q_m$ (mg/g)	$K_L$ (L/mg)	$R^2$	$\chi^2$	$K_f$ (mg/g)	$n$	$R^2$	$\chi^2$
CBA	10–100	15.25	0.0257	0.9923	13.6	1.04	1.8859	0.9721	73.4
SSZ-13		26.79	0.0124	0.9962	32.7	0.64	1.4125	0.9214	92.5
CBA	100–1000	49.26	0.0071	0.9931	23.6	4.655	2.9792	0.9554	94.5
SSZ-13		210.75	0.0258	0.9899	72.3	34.39	3.4246	0.9005	138.2

**Table 4**  
Summary of the literature on the separation of ARS by various adsorbents.

Adsorbent	pH	Adsorption capacity (mg/g)	Initial dye concentration	Reference
Magnetic chitosan	3	40.12	50, 100 mmol/mL	(Fan et al., 2012)
Activated carbon	1	<20	45–100 mg/L	(Ghaedi et al., 2011)
Mustard husk	3	1.97	25, 50, 100 mg/L	(Gautam et al., 2013)
Gold nanoparticles AC	4	123.4	35, 45 mg/L	(Roosta et al., 2014)
Modified nano-sized silica	2	200	50–1000 mg/L	(Li et al., 2011)
MAC nano-composite	2	108.6	10–200 mg/L	(Fayazi et al., 2015)
Activated carbon	6	8.29	200– 600 mg/L	(Bhomick et al., 2020)
Porous xerogels	2	30.8	–	(Wu et al., 2004)
Hydroxyapatite	2	34.2	5–80 ppm	(Piri et al., 2019)
APTES grafted sonicated vermiculate	2	18.2	0.0033 – 0.1 mmol/L	(Ali et al., 2020)
Polypyrrole-coated magnetic nanoparticles	4	53.66	10–130 mg/L	(Gholivand et al., 2015)
CBA	2	49.26	100–1000 mg/L	This work
SSZ-13	3	210.75	100–1000 mg/L	This work

$$\text{Nonlinear Pseudo - second - order : } q_t = \frac{q_e^2 k_2 t}{1 + q_e k_2 t} \quad (9)$$

$$\text{Nonlinear Elovich } q_t = \frac{1}{\beta} \ln(1 + \alpha \beta t) \quad (10)$$

where  $q_e$  and  $q_t$  (mg/g) are the amount of the dye adsorbed by the CBA, and SSZ-13 the equilibrium time  $t$  respectively,  $k_1, k_2$  are the rate constants for the pseudo-first and pseudo-second order kinetic models,  $\alpha, \beta$  are the rate of initial adsorption (mg/g/min), and desorption constant (mg/g) respectively. The pseudo-first-order and pseudo-second-order kinetic plots for the sorption of ARS dye onto CBA and SSZ-13 adsorbents at variable concentrations under a constant temperature of 298 K are shown in Fig. 6(a–h). Further, a summary of the experimental and the calculated kinetic parameters are listed in Table 5. For both the

adsorbents CBA, and SSZ-13, the kinetics were best defined in the pseudo-second-order kinetic model, as the values of  $q_{e,cal} = 196.5$  mg/g were closer to the  $q_{e,exp} = 195.11$  mg/g for SSZ-13,  $q_{e,exp} = 45.39$  mg/g is more relative to the  $q_{e,cal} = 44.35$  mg/g, and the correlation coefficients obtained are greater than 0.99 for both the adsorbents. In addition, variable concentrations often suit well in the case of pseudo-second-order kinetic models. They tend to show better dye uptake capacity than the pseudo-first-order kinetic model. Besides, Elovich kinetic model is to define the second order chemisorption with an assumption of the solid systems are energetically heterogeneous in nature (Thirunavukkarasu et al., 2018). Table 5 shows the increasing value of  $\alpha$ , and decreasing value of  $\beta$  with the increasing concentration for both the adsorbents CBA and SSZ-13. Thus lowering behavior of  $\beta$  with the rise in initial adsorbate concentration at variable time depicted the chemisorptive behavior of ARS dye onto the CBA and SSZ-13. Therefore, for the current analysis, the pseudo-second-order kinetics fitted well compared to the pseudo-first-order, and the Elovich kinetic model confirming the rate-limiting step is chemisorption (Gomri et al., 2018), i. e., the exchange or sharing of electrons via valence forces.

### 3.16. Temperature Influence

Temperature is another necessary parameter influencing the adsorption process. Increasing temperature in the adsorption medium contributes to an increase in the rate of diffusion across the external boundary layer of the adsorbate molecules, thereby reducing the viscosity of the solution. Moreover, temperature affects the adsorbents equilibrium potential and varies with the adsorbate. A series of experiments were performed in the present study by varying temperatures with an initial dye concentration of 300 mg/L in the range of 295–330 K, maintaining pH = 2 for CBA and pH = 3 for SSZ-13 (Fig. 7a). With the increase in the temperature, the adsorption capacity increased from 24.74 mg/g to 36.56 mg/g for CBA; while SSZ-13 reported 99.7–113.2 mg/g. The increase in the uptake capacity with the temperature is an indication of the endothermic nature of the reaction (Zhou et al., 2015) due to the stable active sites and the augmented mobility of the ions facilitating the formation of monolayer surface, i.e., confirmed by the Langmuir model (Yang et al., 2017).

### 3.17. Thermodynamic studies

The thermodynamic parameters such as Gibbs free energy, entropy, enthalpy variations defines the possibility, spontaneity, and nature of

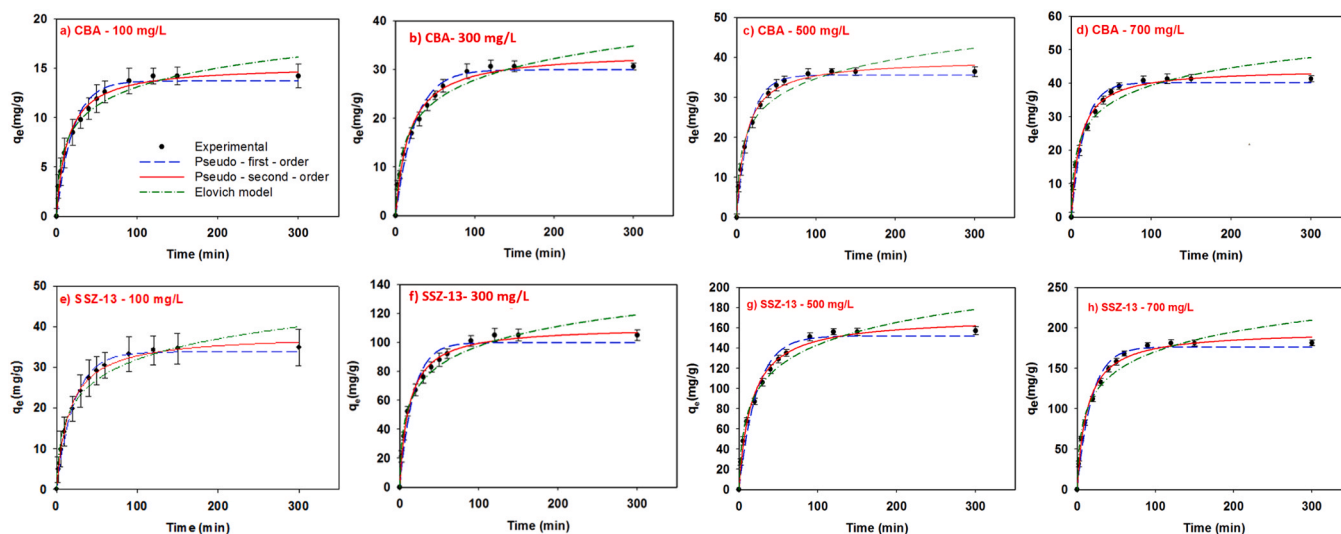


**Fig. 6.** Nonlinear kinetic studies varied with dye concentration (a-d) CBA, (e-h) SSZ-13.

**Table 5**  
Kinetic modeling of data for the separation of ARS using CBA, and SSZ-13.

Adsorbent	Conc. (mg/L)	$q_{e, exp}$ (mg/g)	Pseudo-first-order model			Pseudo-second-order model			Elovich kinetic model		
			$q_{e1, cal}$ (mg/g)	$k_1$ (1/min)	$R^2$	$q_{e2, cal}$ (mg/g)	$k_2$ (g/mg min)	$R^2$	$\alpha$ (mg/g/min)	$\beta$ (g/mg)	$R^2$
CBA	100	14.87	11.72	0.0411	0.9661	15.29	0.0017	0.9918	3.039	0.3589	0.9733
	300	32.61	29.96	0.0495	0.9699	33.69	0.0021	0.9942	4.873	0.1560	0.9709
	500	38.74	31.53	0.0609	0.9832	39.45	0.0023	0.9938	10.262	0.1442	0.9558
	700	45.39	38.16	0.0630	0.9718	44.35	0.0027	0.9917	13.308	0.1314	0.9601
SSZ-13	100	39.21	31.81	0.0455	0.9866	38.15	0.0002	0.9962	5.6285	0.1362	0.9685
	300	110.39	89.83	0.0445	0.9642	111.08	0.0005	0.9933	27.347	0.0507	0.9754
	500	168.89	152.11	0.0547	0.9723	170.62	0.0008	0.9906	27.2237	0.0311	0.9739
	700	195.11	176.55	0.0588	0.9787	196.57	0.0016	0.9949	42.8956	0.0281	0.9628

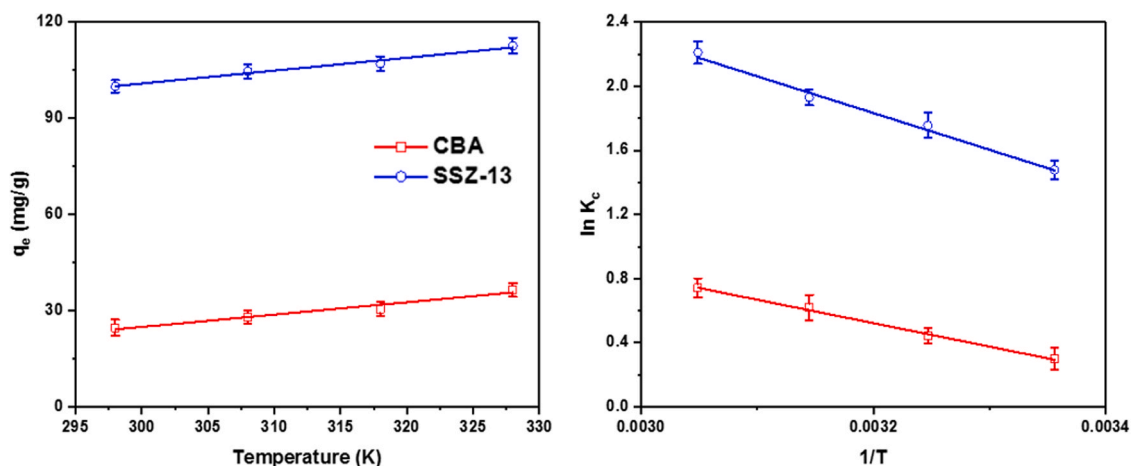


Fig. 7. (a) Effect of temperature on the adsorption of ARS dye onto CBA, and SSZ-13, (b) Van't Hoff plot for the adsorption of ARS dye onto the CBA, and SSZ-13.

adsorption on inherent energetic changes. The following equations evaluate all these parameters mentioned above, Eqs. (11–14):

$$\Delta G^\circ = -RT \ln K_c \quad (11)$$

$$K_c = \frac{C_{Ae}}{C_e} \quad (12)$$

$$\Delta G^\circ = \Delta H^\circ - T\Delta S^\circ \quad (13)$$

$$\ln K_c = -\frac{\Delta G^\circ}{RT} = -\frac{\Delta H^\circ}{RT} + \frac{\Delta S^\circ}{R} \quad (14)$$

where  $C_{Ae}$ , is the solid phase concentration at equilibrium mg/L,  $C_e$  is the equilibrium concentration of dye solution mg/L,  $R$  is the universal gas constant,  $T$  is the absolute temperature,  $K_c$  is the distribution constant, and the values  $\Delta H^\circ$ , and  $\Delta S^\circ$  were the intercept and slope of the plot  $\ln K_c$  vs  $1/T$  (Fig. 7b) as per the Van't Hoff equation. From the Table 6 it is evident that the value of the Gibbs free energy for both the sorbents CBA, and SSZ-13 was found to be negative for all the studied temperature conditions, representing the sorption process is spontaneous. Moreover, the enthalpy and the entropy changes reported being

**Table 6**  
Thermodynamic assessment on adsorption of ARS onto CBA, and SSZ-13.

Adsorbent	Temp. (K)	$\Delta G^\circ$ (kJ/mol)	$\Delta H^\circ$ (kJ/mol)	$\Delta S^\circ$ (kJ/mol K)
CBA	298	-0.7491		
	308	-1.1373		
	318	-1.6379	12.13	0.043
	328	-2.0219		
SSZ-13	298	-3.6606		
	308	-4.4974		
	318	-5.1036	19.25	0.077
	328	-6.0255		

positive for both the sorbents signifying the adsorption process is endothermic (Hossini Asl et al., 2020). Besides, the positive quantities of entropy indicates the increasing the randomness at the solid-liquid interface (Batoool et al., 2018) during the sorption of ARS dye onto the CBA, and SSZ-13.

#### 4. Adsorption mechanism

It is known that the most common interaction of the adsorbent and the adsorbate is via electrostatic attraction, hydrogen bonding,  $\pi$ - $\pi$  interactions, Van der Waals interactions, ion-exchange etc. But, in the present study, the anionic ARS dye was adsorbed onto the surface of the cationic medium zeolite SSZ-13 was mainly due to the electrostatic interactions shown in Fig. 8. These electrostatic interactions are resultant of the silanol groups (Si-OH) in both CBA, and SSZ-13. On the other hand, based on the previous studies, ARS dye is an anthraquinone anionic dye, having a pKa value of 4.5; thus ARS exhibits positive charge in acidic medium, i.e., pH = 3.5. At lower pH values, CBA, and SSZ-13 may readily receive a proton to form a positive group ( $-\text{NH}_3^+$ ) while the ARS could lose a proton to create a negative group ( $-\text{SO}_3^-$ ) (Piri et al., 2019). The interaction between the CBA, SSZ-13, and ARS is therefore regulated by the electrostatic attraction between the corresponding groups ( $-\text{NH}_3^+$ ) and  $-\text{SO}_3^-$ . In addition, lower pH results in an increase in the number of reaction sites for ( $\text{NH}_3^+$ ) and  $-\text{SO}_3^-$ , thus increasing the adsorption of ARS on to CBA, and SSZ-13. Further, increasing the pH and migrating towards the alkaline medium, the adsorption tendency is decreased due to the reduction in the number of active, positive sites on the adsorbent, increasing negative sides causing electrostatic repulsion between adsorbent and adsorbate. Thus pH is the regulating factor in assessing the dissociation of the functional groups, active sites of the adsorbents, and hence augmented adsorption tendency is seen acidic medium or lower pH values (pH = 2 for CBA, pH = 3 for SSZ-13). The basic objective of fusion followed by hydrothermal treatment is to break

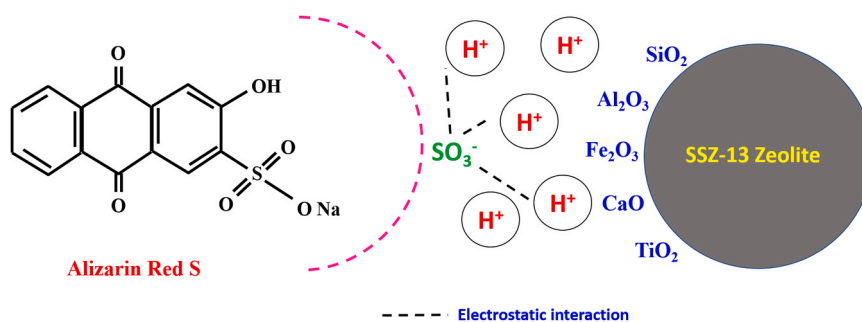


Fig. 8. Adsorption mechanism of ARS dye onto SSZ-13.

the unorganized structure of CBA and repolymerize to pure phase zeolite crystals which is SSZ-13 in the present scenario confirmed from SEM micrographs. Further, the published literature on the Si/Al ratio of the SSZ-13 zeolites reported high values possessing better thermal stability. However, for adsorption reactions on batch mode at room temperatures favors dealumination or low Si/Al ratio (Abraham et al., 2004). From Table 1 it is seen that the Si/Al ratio has been decreased from 5 to 2.5 and from the adsorption tests, we can observe the adsorption efficiency is higher for SSZ-13 after hydrothermal treatment rather than high Si/Al ratio of CBA.

## 5. Desorption studies

Desorption studies provide key information related to the possibility of sorbent recovery and reuse. Primarily, adsorption tests were performed by taking 30 mL of the 300 mg/L dye solution, adding 0.03 g of the adsorbent (CBA, and SSZ-13), maintaining the optimal pH of 2 and 3 for CBA and SSZ-13 at 298 K and agitated at 200 rpm for 120 min. After the completion of the adsorption, the solution was dried in a furnace at 333 K, and sediment was recovered for the desorption studies. For the desorption studies of ARS onto CBA, and SSZ-13 adsorbents, suitable eluents 0.1 M NaOH, 0.1 M HCl, 100% ethanol, 0.1 M HCl/EtOH, and 0.1 M NaOH/EtOH were chosen. The choice of eluents spans over-acidic, alkaline and organic materials to evaluate the desorption under various environments. From Fig. 9(a) it is observed that the combination of NaOH/EtOH reported significant desorption efficiency of 92% CBA, and 96% SSZ-13 followed by NaOH (81% CBA, and 88% SSZ-13), ethanol (66% CBA, and 75% SSZ-13), 0.1 M HCl (59% CBA, and 44% SSZ-13), and finally 0.1 M HCl/EtOH (54% CBA, and 69% SSZ-13). This showed that the alkaline desorbing agents highly favors the selected combination of dye and the sorbents when compared to the acidic and organic eluents. The higher desorption using NaOH has ascribed due to the hydroxyl groups interacting with the adsorbing surface sites. It replaces the anionic dye resulting in the much more negative surface charge and repulsion of dye molecules followed by the detachment of

the sorbent (Sadaf et al., 2015). Thus, the maximum recovery is seen in the case of 0.1 M NaOH/EtOH among the selected eluents/desorbing agents.

## 6. Regeneration studies

The regeneration and reusability of the adsorbent solely depend on adsorption-desorption characteristics. It is not always a demand for process economy, but commercial scaling and viability is a function of the material (adsorbate) reusability. Thus, adsorption-desorption studies are mandatory to regenerate the active binding sites for reusability. Hence, in the present study, adsorption-desorption experiments were conducted using 0.1 M NaOH/EtOH for the successive five cycles of adsorption and desorption using both the adsorbents CBA Fig. 9(b), SSZ-13 Fig. 9(c). For the adsorbent CBA, the adsorption-desorption capacity showed a declining pattern from 81% to 68% (adsorption), 92–81% (desorption) for five successive cycles. Whereas, the case of SSZ-13 reported similar decreasing trend with the number of cycles, and the capacity of adsorption-desorption shrank from 88% to 75% (adsorption), 96–83% (desorption). From the studies mentioned above, it can be seen that the adsorbent SSZ-13 can be regenerated and reused for a minimum of five cycles, CBA can be used for two cycles to adsorb anionic ARS dye molecules successively.

## 7. Conclusion

In the present study, a low-cost, eco-friendly, greater sorption featured zeolite SSZ-13 was synthesized from CBA via hydrothermal method. Further, the research showed the importance of hydrothermal treatment lead to 30 folds increase in the surface area of newly synthesized zeolite SSZ-13 (206.6 m<sup>2</sup>/g) when compared to the raw CBA (7.81 m<sup>2</sup>/g). Batch sorption studies were performed to assess the efficiency of SSZ-13, raw CBA towards the anionic ARS dye. The Langmuir model explained the ARS adsorption well and calculated the maximum adsorption efficiency of 210.75 mg/g in case of SSZ-13, while it is

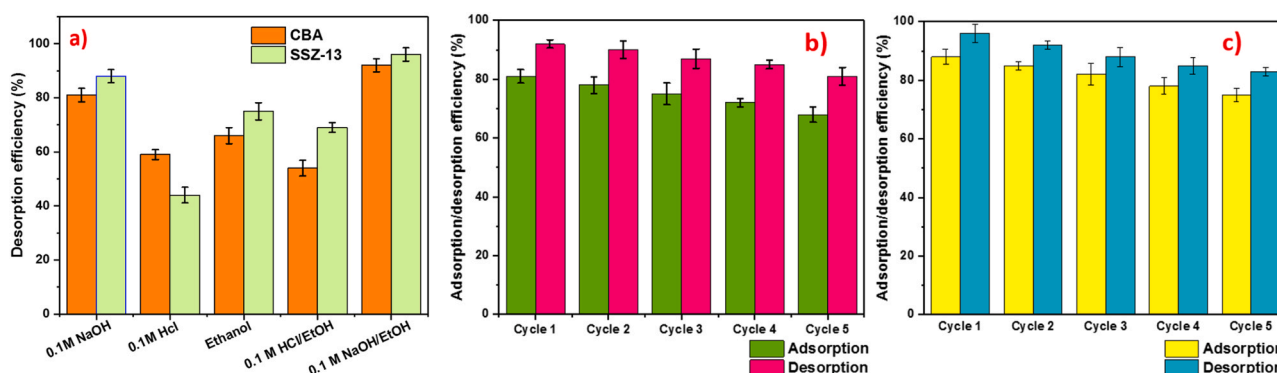


Fig. 9. (a) Effect of Eluents on desorption of CBA, and SSZ-13, (b) reusability of CBA, (c) reusability of zeolite SSZ-13.

49.26 mg/g using raw CBA as adsorbent. Further, the dye uptake onto the adsorbent was tested in the light of kinetics revealed that adsorption of ARS onto the CBA, and SSZ-13 followed the pseudo-second-order kinetic model. In addition, the rate limiting step of chemisorption was confirmed by the Elovich kinetic model. The adsorption thermodynamics revealed the adsorption phenomenon is spontaneous, and endothermic in nature. From the desorption studies, it was understood that a combination of NaOH/EtOH resulted in the best desorption of CBA (92%), and SSZ-13 (96%) in comparison to the other selected elements. Finally, the regeneration studies revealed that the adsorbent CBA did well during the first two cycles with no significant drop in sorption of ARS dye. Whereas, SSZ-13 performed well until five cycles and declined after that. In summary, a successful conversion of eco-toxic CBA to technically feasible SSZ-13 zeolite via hydrothermal treatment could be a new entrant in zeolite product base for the sorption of anionic dye ARS from effluent streams.

### CRedit authorship contribution statement

**Anjani R.K. Gollakota:** Conceptualization, Methodology, Formulation, Experimentation, Analysis, Validation, Writing - original draft, Editing. **Munagapati Venkata Subbaiah:** Conceptualization, Data curation. **Vikranth Volli:** Formal analysis. **Sneha Gautam:** Editing. **Jet-Chau Wen:** Conceptualization, Validation. **Chi-Min Shu:** Supervision, Conceptualization, Editing, Resources.

### Declaration of Competing Interest

The authors declare that they have no known competing financial interests or personal relationships that could have appeared to influence the work reported in this paper.

### Acknowledgements

The authors sincerely appreciate the help and cooperation of PS&DPL group.

### Appendix A. Supporting information

Supplementary data associated with this article can be found in the online version at [doi:10.1016/j.jhazmat.2021.125925](https://doi.org/10.1016/j.jhazmat.2021.125925).

### References

- Abbas, M., Adil, M., Ehtisham-ul-Haque, S., Munir, B., Yameen, M., Ghaffar, A., Shar, G. A., Tahir, M., Asif, Iqbal, M., 2018. Vibrio fischeri bioluminescence inhibition assay for ecotoxicity assessment: a review. *Sci. Total Environ.* 626, 1295–1309. <https://doi.org/10.1016/j.scitotenv.2018.01.066>.
- Abraham, A., Lee, S.H., Shin, C.H., Hong, S.B., Prins, R., VanBokhoven, J.A., 2004. Influence of framework silicon to aluminium ratio on aluminium coordination and distribution in zeolite Beta investigated by 27Al MAS and 27Al MQ MAS NMR. *Phys. Chem. Chem. Phys.* 6, 3031–3036. <https://doi.org/10.1039/b401235f>.
- Adeyemo, A.A., Adeoye, I.O., Bello, O.S., 2017. Adsorption of dyes using different types of clay: a review. *Appl. Water Sci.* 7, 543–568. <https://doi.org/10.1007/s13201-015-0322-y>.
- Ali, N., Ali, F., Ullah, I., Ali, Z., Duclaux, L., Reinert, L., Lévêque, J.M., Farooq, A., Bilal, M., Ahmad, I., 2020. Organically modified micron-sized vermiculite and silica for efficient removal of Alizarin Red S dye pollutant from aqueous solution. *Environ. Technol. Innov.* 19, 101001 <https://doi.org/10.1016/j.eti.2020.101001>.
- Argiz, C., Sanjuán, M.A., Menéndez, E., 2017. Coal bottom ash for portland cement production. *Adv. Mater. Sci. Eng.* 2017 (2017), 1–7. <https://doi.org/10.1155/2017/6068286>.
- Armbruster, M.H., Austin, J.B., 1938. The adsorption of gases on plane surfaces of mica. *J. Am. Chem. Soc.* 60, 467–475. <https://doi.org/10.1021/ja01269a066>.
- Austin Taylor, H., Thon, N., 1952. Kinetics of chemisorption. *J. Am. Chem. Soc.* 74, 4169–4173. <https://doi.org/10.1021/ja01136a063>.
- Barrer, R.M., 2007. *Hydrothermal Chemistry of Zeolites*. Academic Press, London, United Kingdom.
- Bärtsch, M., Bornhauser, P., Calzaferri, G., Imhof, R., 1994. H<sub>8</sub>Si<sub>8</sub>O<sub>12</sub>: a model for the vibrational structure of zeolite A. *J. Phys. Chem.* 98, 2817–2831. <https://doi.org/10.1021/j100062a016>.

- Batool, F., Akbar, J., Iqbal, S., Noreen, S., Bukhari, S.N.A., 2018. Study of isothermal, kinetic, and thermodynamic parameters for adsorption of cadmium: an overview of linear and nonlinear approach and error analysis. *Bioinorg. Chem. Appl.* 2018 (2018), 1–11. <https://doi.org/10.1155/2018/3463724>.
- Belskaya, O.B., Danilova, I.G., Kazakov, M.O., Mironenko, R.M., Lavrenov, A.V., Likhobolov, V.A., 2012. FTIR spectroscopy of adsorbed probe molecules for analyzing the surface properties of supported Pt (Pd) catalysts, infrared spectroscopy. *Mater. Sci. Eng. Technol.* 20 <https://doi.org/10.5772/36275>.
- Benhouria, A., Islam, M.A., Zaghouane-Boudiaf, H., Boutahala, M., Hameed, B.H., 2015. Calcium alginate-bentonite-activated carbon composite beads as highly effective adsorbent for methylene blue. *Chem. Eng. J.* 270, 621–630. <https://doi.org/10.1016/j.cej.2015.02.030>.
- Bhomick, P.C., Supong, A., Baruah, M., Pongener, C., Gogoi, C., Sinha, D., 2020. Alizarin Red S adsorption onto biomass-based activated carbon: optimization of adsorption process parameters using Taguchi experimental design. *Int. J. Environ. Sci. Technol.* 17, 1137–1148. <https://doi.org/10.1007/s13762-019-02389-1>.
- Bieseki, L., Penha, F.G., Pergher, S.B.C., 2013. Zeolite synthesis employing a Brazilian coal ash as the silicon and aluminum source and its applications in adsorption and pigment formulation. *Mater. Res.* 16, 38–43. <https://doi.org/10.1590/S1516-14392012005000144>.
- Bing, L., Liu, J., Yi, K., Li, F., Han, D., Wang, F., Wang, G., 2020. Rapid synthesis of hierarchical SSZ-13 zeolite microspheres: via a fluoride-assisted in situ growth route using aluminum isopropoxide as aluminum source. *RSC Adv.* 10, 3566–3571. <https://doi.org/10.1039/c9ra08895d>.
- Blackburn, R.S., 2004. Natural polysaccharides and their interactions with dye molecules: applications in effluent treatment. *Environ. Sci. Technol.* 38, 4905–4909. <https://doi.org/10.1021/es049972n>.
- Breck, D.W., 1974. *Zeolite Molecular Sieves: Structure Chemistry, first ed.* John Wiley and Sons, New York, USA.
- Bruzzese, P.C., Pyra, K., Bertmer, M., Kinga, G., Poppitz, D., Pöpl, A., Gläser, R., 2020. Nanosized Cu-SSZ-13 and its application in NH<sub>3</sub>-SCR. *Catalysts* 10, 506.
- Chowdhury, S., Mishra, R., Saha, P., Kushwaha, P., 2011. Adsorption thermodynamics, kinetics and isosteric heat of adsorption of malachite green onto chemically modified rice husk. *Desalination* 265, 159–168. <https://doi.org/10.1016/j.desal.2010.07.047>.
- Daniel Abraham, S., Theodore David, S., Biju Bennie, R., Joel, C., Sanjay Kumar, D., 2016. Eco-friendly and green synthesis of BiVO<sub>4</sub> nanoparticle using microwave irradiation as photocatalyst for the degradation of Alizarin Red S. *J. Mol. Struct.* 1113, 174–181. <https://doi.org/10.1016/j.jmolstruc.2016.01.053>.
- Datka, J., Tuznik, E., 1985. Hydroxyl groups and acid sites in NaZSM-5 zeolites studied by i.r. spectroscopy. *Zeolites* 5, 230–232. [https://doi.org/10.1016/0144-2449\(85\)90092-2](https://doi.org/10.1016/0144-2449(85)90092-2).
- Dewi, R., Agusnar, H., Alfian, Z., Tamrin, 2018. Characterization of technical kaolin using XRF, SEM, XRD, FTIR and its potentials as industrial raw materials. *J. Phys. Conf. Ser.* 1116, 8–14. <https://doi.org/10.1088/1742-6596/1116/4/042010>.
- Fan, L., Zhang, Y., Li, X., Luo, C., Lu, F., Qiu, H., 2012. Removal of alizarin red from water environment using magnetic chitosan with Alizarin Red as imprinted molecules. *Colloids Surf. B Biointerfaces* 91, 250–257. <https://doi.org/10.1016/j.colsurfb.2011.11.014>.
- Fayazi, M., Ghanei-Motlagh, M., Taher, M.A., 2015. The adsorption of basic dye (Alizarin red S) from aqueous solution onto activated carbon/γ-Fe<sub>2</sub>O<sub>3</sub> nanocomposite: kinetic and equilibrium studies. *Mater. Sci. Semicond. Process.* 40, 35–43. <https://doi.org/10.1016/j.mssp.2015.06.044>.
- Ferone, C., Esposito, S., Pansini, M., 2005. Thermally induced structural and microstructural evolution of barium exchanged zeolite a to celonian. *Stud. Surf. Sci. Catal.* 155, 249–260. [https://doi.org/10.1016/s0167-2991\(05\)80153-3](https://doi.org/10.1016/s0167-2991(05)80153-3).
- Freundlich, V.H., 1907. Kolloidfüllung und adsorption. *Juretzka Gattierung Von. Zinkblende Und Galmei* 20, 750–754. <https://doi.org/10.1002/ange.19070201806>.
- Gautam, R.K., Mudhoo, A., Chattopadhyaya, M.C., 2013. Kinetic, equilibrium, thermodynamic studies and spectroscopic analysis of Alizarin Red S removal by mustard husk. *J. Environ. Chem. Eng.* 1, 1283–1291. <https://doi.org/10.1016/j.jece.2013.09.021>.
- Geobaldo, F., Fiorilli, S., Onida, B., Giordano, G., Katovic, A., Garrone, E., 2003. An FTIR study of zeolite theta-1. *J. Phys. Chem. B* 107, 1258–1262. <https://doi.org/10.1021/jp026354p>.
- Ghaedi, M., Hassanzadeh, A., Kokhdan, S.N., 2011. By treating MWCNTs with ball milling. *J. Chem. Eng. Data.* 56, 2511–2520.
- Ghasemi, Z., Younesi, H., 2012. Preparation of free-template nanometer-sized Na-A and -X zeolites from rice husk ash. *Waste Biomass-Valoriz.* 3, 61–74. <https://doi.org/10.1007/s12649-011-9084-4>.
- Gholivand, M.B., Yamini, Y., Dayeni, M., Seidi, S., Tahmasebi, E., 2015. Adsorptive removal of alizarin red-S and alizarin yellow GG from aqueous solutions using polypyrrole-coated magnetic nanoparticles. *J. Environ. Chem. Eng.* 3, 529–540. <https://doi.org/10.1016/j.jece.2015.01.011>.
- Gollakota, A.R.K., Volli, V., Shu, C.M., 2019. Progressive utilisation prospects of coal fly ash: a review. *Sci. Total Environ.* 672, 951–989. <https://doi.org/10.1016/j.scitotenv.2019.03.337>.
- Gollakota, A.R.K., Volli, V., Venkata, S., 2020. Munagapati, Jet-Chau Wen, Chi-Min Shu. Synthesis of novel ZSM-22 zeolite from Taiwanese coal fly ash for the selective separation of Rhodamine 6G. *J. Mater. Res. Technol.* 9, 15381–15393. <https://doi.org/10.1016/j.jmrt.2020.10.070>.
- Gomri, F., Finqueneisel, G., Zimny, T., Korili, S.A., Gil, A., Boutahala, M., 2018. Adsorption of Rhodamine 6G and humic acids on composite bentonite-alginate in single and binary systems. *Appl. Water Sci.* 8, 156. <https://doi.org/10.1007/s13201-018-0823-6>.

- Guo, C., Zou, J., Ma, S., Yang, J., Wang, K., 2019. Alumina extraction from coal fly ash via low-temperature potassium bisulfate calcination. *Minerals* 9 (10), 585. <https://doi.org/10.3390/min9100585>.
- Haghsereht, F., Nouri, S., Lu, G.Q., 2002. Effects of the solute ionization on the adsorption of aromatic compounds from dilute aqueous solutions by activated carbon. *Langmuir* 18, 1574–1579. <https://doi.org/10.1021/la010903l>.
- Haroon, M., Wang, L., Yu, H., Ullah, R.S., Zain-ul-Abdin, Khan, R.U., Chen, Q., Liu, J., 2018. Synthesis of carboxymethyl starch-g-polyvinylpyrrolidones and their properties for the adsorption of Rhodamine 6G and ammonia. *Carbohydr. Polym.* 186, 150–158. <https://doi.org/10.1016/j.carbpol.2018.01.052>.
- Hartmann, A., Buhl, J.C., Lutz, W., 2012. Synthesis and properties of zeolites from autoclaved aerated concrete (AAC) waste. *Z. Fur Anorg. Und Allg. Chem.* 638, 1297–1306. <https://doi.org/10.1002/zaac.201200175>.
- Ho, Y.S., McKay, G., 1999. Pseudo-second order model for sorption processes. *Process Biochem* 34, 451–465. <https://doi.org/10.1021/acs.oprd.7b00090>.
- Hossini Asl, S.M., Masomi, M., Tajbakhsh, M., 2020. Hybrid adaptive neuro-fuzzy inference systems for forecasting benzene, toluene & m-xylene removal from aqueous solutions by HZSM-5 nano-zeolite synthesized from coal fly ash. *J. Clean. Prod.* 258, 120688. <https://doi.org/10.1016/j.jclepro.2020.120688>.
- Iqbal, M., 2016. Vicia faba bioassay for environmental toxicity monitoring: a review. *Chemosphere* 144, 785–802. <https://doi.org/10.1016/j.chemosphere.2015.09.048>.
- Iqbal, M., Abbas, M., Nisar, J., Nazir, A., 2019. Bioassays based on higher plants as excellent dosimeters for ecotoxicity monitoring: a review. *Chem. Int.* 5, 1–80. <https://doi.org/10.31221/osf.io/z2ynn>.
- Jabeen, S., Shah, M.T., Ahmed, I., Khan, S., Hayat, M.Q., 2014. Physico-chemical parameters of surface and ground water and their environmental impact assessment in the Haripur Basin, Pakistan. *J. Geochem. Explor.* 138, 1–7. <https://doi.org/10.1016/j.gexplo.2013.12.004>.
- Karthick, K., Namasivayam, C., Pragasam, L.A., 2018. Kinetics and isotherm studies on acid dye adsorption using thermal and chemical activated *Jatropha* husk carbons. *Environ. Prog. Sustain. Energy* 37, 719–732. <https://doi.org/10.1002/ep.12745>.
- Katara, S., 2014. Surface modification of fly ash by thermal activation: a DR/FTIR study. *Int. Res. J. Pure Appl. Chem.* 3, 299–307. <https://doi.org/10.9734/irjpac/2014/4287>.
- Khosa, M.A., Shah, S.S., Nazar, M.F., 2011. UV-visible spectrometric study and micellar enhanced ultrafiltration of Alizarin Red S dye. *J. Dispers. Sci. Technol.* 32, 1634–1640. <https://doi.org/10.1080/01932691.2010.528338>.
- Kuzmickas, L., Andrade, F.R.D., Szabó, G.A.J., Motta, J.F.M., Cabral, M., 2013. Influence of diopside: feldspar ratio in ceramic reactions assessed by quantitative phase analysis (X-ray diffraction – Rietveld method). *Ceramica* 59, 345–350. <https://doi.org/10.1590/S0366-69132013000200022>.
- Lagergren, S., 1989. Zur theorie der sogenannten adsorption gloster stoffe. *K. Sven. Vetensk. Handl.* 24, 1–39.
- Li, D., Liu, Q., Ma, S., Chang, Z., Zhang, L., 2011. Adsorption of alizarin red S onto nano-silica modified with  $\gamma$ -aminopropyltriethoxysilane. *Adsorpt. Sci. Technol.* 29, 289–300. <https://doi.org/10.1260/02636174.29.3.289>.
- Li, K.M., Jiang, J.G., Tian, S.C., Chen, X.J., Yan, F., 2014. Influence of silica types on synthesis and performance of amine-silica hybrid materials used for CO<sub>2</sub> capture. *J. Phys. Chem. C* 118, 2454–2462. <https://doi.org/10.1021/jp408354r>.
- Li, Z., Navarro, M.T., Martínez-Triguero, J., Yu, J., Corma, A., 2016. Synthesis of nano-SSZ-13 and its application in the reaction of methanol to olefins. *Catal. Sci. Technol.* 6, 5856–5863. <https://doi.org/10.1039/c6cy00433d>.
- Machado, F.M., Carmalin, S.A., Lima, E.C., Dias, S.L.P., Prola, L.D.T., Saucier, C., Jauris, I.M., Zanella, I., Fagan, S.B., 2016. Adsorption of Alizarin Red S dye by carbon nanotubes: an experimental and theoretical investigation. *J. Phys. Chem. C* 120, 18296–18306. <https://doi.org/10.1021/acs.jpcc.6b03884>.
- Madrakian, T., Afkhami, A., Ahmadi, M., Bagheri, H., 2011. Removal of some cationic dyes from aqueous solutions using magnetic-modified multi-walled carbon nanotubes. *J. Hazard. Mater.* 196, 109–114. <https://doi.org/10.1016/j.jhazmat.2011.08.078>.
- Mainganye, D., 2012. Synthesis of zeolites from South African coal fly ash: Investigation of scale-up conditions. pp. 1–114.
- Mandal, K., Gu, Y., Westendorff, K.S., Li, S., Pihl, J.A., Grabow, L.C., Epling, W.S., Paolucci, C., 2020. Condition-dependent Pd speciation and NO adsorption in Pd/Zeolites. *ACS Catal.* 10, 12801–12818. <https://doi.org/10.1021/acscatal.0c03585>.
- Metin, A.Ü., Çiftçi, H., Alver, E., 2013. Efficient removal of acidic dye using low-cost biocomposite beads. *Ind. Eng. Chem. Res.* 52, 10569–10581. <https://doi.org/10.1021/ie400480s>.
- Milinic, J., Dias, Á.A., Janeiro, A.I., Pereira, M.F.C., Martins, S., Petersen, S., Barriga, F.J.A.S., 2020. XRD identification of ore minerals during cruises: refinement of extraction procedure with sodium acetate buffer. *Minerals* 10, 160. <https://doi.org/10.3390/min10020160>.
- Mittala, A., Gupta, V.K., 2010. Adsorptive removal and recovery of the azo dye eriochrome black T. *Toxicol. Environ. Chem.* 92, 1813–1823. <https://doi.org/10.1080/02772248.2010.485998>.
- Murayama, N., Yamamoto, H., Shibata, J., 2002. Mechanism of zeolite synthesis from coal fly ash by alkali hydrothermal reaction. *Int. J. Miner. Process.* 64, 1–17. [https://doi.org/10.1016/S0301-7516\(01\)00046-1](https://doi.org/10.1016/S0301-7516(01)00046-1).
- Neville, N.Z., 2016. Synthesis of zeolite (ZSM-5 and Faujasite) and geopolymer from South African coal fly ash By.
- Nielsen, M., Brogaard, R.Y., Falsig, H., Beato, P., Swang, O., Svelle, S., 2015. Kinetics of zeolite dealumination: insights from H-SSZ-13. *ACS Catal.* 5, 7131–7139. <https://doi.org/10.1021/acscatal.5b01496>.
- Nishi, J., Thompson, R.W., 2002. Synthesis of classical zeolites. In: Schuth, F., Sing, K.S.W., Weitkamp, J. (Eds.), *Handb. Porous Solids, second ed.* Wiley-VCH Verlag GmbH, Weinheim, Germany, p. 70.
- Patrick, D.O., Yusup, S., Osman, N.B., Zabiri, H., Shahbaz, M., 2017. Performance of water-leached coal bottom ash as catalyst in Thermogravimetric Analyser (TGA) biomass gasification. *Chem. Eng. Trans.* 61, 1681–1686. <https://doi.org/10.3303/CET1761278>.
- Pham, T.D., Liu, Q., Lobo, R.F., 2013. Carbon dioxide and nitrogen adsorption on cation-exchanged SSZ-13 zeolites. *Langmuir* 29, 832–839. <https://doi.org/10.1021/la304138z>.
- Piri, F., Mollahosseini, A., Khadir, A., Hosseini, M.Milani, 2019. Enhanced adsorption of dyes on microwave-assisted synthesized magnetic zeolite-hydroxyapatite nanocomposite. *J. Environ. Chem. Eng.* 7, 103338. <https://doi.org/10.1016/j.jece.2019.103338>.
- Pourjavadi, A., Nazari, M., Hosseini, S.H., 2015. Synthesis of magnetic graphene oxide-containing nanocomposite hydrogels for adsorption of crystal violet from aqueous solution. *RSC Adv.* 5, 32263–32271. <https://doi.org/10.1039/c4ra17103a>.
- Proding, S., Vemuri, R.S., Varga, T., Peter McGrail, B., Motkuri, R.K., Derewinski, M.A., 2016. Impact of chabazite SSZ-13 textural properties and chemical composition on CO<sub>2</sub> adsorption applications. *New J. Chem.* 40, 4375–4385. <https://doi.org/10.1039/c5nj03205a>.
- Querol, X., 2002. Synthesis of zeolites from coal fly ash: an overview. *Int. J. Coal Geol.* 50, 413–423. [https://doi.org/10.1016/S0166-5162\(02\)00124-6](https://doi.org/10.1016/S0166-5162(02)00124-6).
- Roosta, M., Ghaedi, M., Mohammadi, M., 2014. Removal of Alizarin Red S by gold nanoparticles loaded on activated carbon combined with ultrasound device: optimization by experimental design methodology. *Powder Technol.* 267, 134–144. <https://doi.org/10.1016/j.powtec.2014.06.052>.
- Sadaf, S., Bhatti, H.N., Arif, M., Amin, M., Nazar, F., 2015. Adsorptive removal of direct dyes by PEI-treated peanut husk biomass: box–Behnken experimental design. *Chem. Ecol.* 31, 252–264. <https://doi.org/10.1080/02757540.2014.950568>.
- Shiau, C.Y., Pan, C.C., 2004. Adsorption of basic dyes from aqueous solution by various adsorbents. *Sep. Sci. Technol.* 39, 1733–1750. <https://doi.org/10.1081/SS-120030779>.
- Shigemoto, N., Hayashi, H., Miyaura, K., 1993. Selective formation of Na-X zeolite from coal fly ash by fusion with sodium hydroxide prior to hydrothermal reaction. *J. Mater. Sci.* 28, 4781–4786. <https://doi.org/10.1007/BF00414272>.
- Sonderam, S., Abd Aziz, A.S., Abdullah, A.H., Mat, R., 2019. Characterisation of NAA zeolite made from Malaysian kaolin. *Chem. Eng. Trans.* 72, 325–330. <https://doi.org/10.3303/CET1972055>.
- Song, Z., Chouparove, E., Jones, K., 2001. FTIR investigation of sediments from NY/NJ Harbor, San Diego Bay, and the Venetian Lagoon, NLS Act. .... 112–116. ([http://www.bnl.gov/isd/documents/23813/Section 2/geological and environmental section/sec2\\_scihi\\_geo\\_song.pdf](http://www.bnl.gov/isd/documents/23813/Section%20geological%20and%20environmental%20section/sec2_scihi_geo_song.pdf)).
- Thirunavukkarasu, A., Muthukumar, K., Nithya, R., 2018. Adsorption of acid yellow 36 onto green nanoceria and amine functionalized green nanoceria: comparative studies on kinetics, isotherm, thermodynamics, and diffusion analysis. *J. Taiwan Inst. Chem. Eng.* 93, 211–225. <https://doi.org/10.1016/j.jtice.2018.07.006>.
- Thommes, M., Kaneko, K., Neimark, A.V., Olivier, J.P., Rodriguez-Reinos, F., Rouquerol, J., Sing, K.S.W., 2015. Physisorption of gases, with special reference to the evaluation of surface area and pore size distribution (IUPAC Technical Report). *Pure Appl. Chem.* 87, 1051–1069. <https://doi.org/10.1515/pac-2014-1117>.
- Wang, Y., Li, Y., Tang, E., 2010. Preparation and characterization of SSZ-13 molecular sieve. *Int. J. Chem.* 2, 128–133. <https://doi.org/10.5539/ijc.v2n1p128>.
- Wang, C., Zhang, Z.W., Liu, H., 2020. Since January 2020 Elsevier has created a COVID-19 resource centre with free information in English and Mandarin on the novel coronavirus COVID-19. The COVID-19 resource centre is hosted on Elsevier Connect, the company's public news and information.
- Ward, C.R., French, D., 2006. Determination of glass content and estimation of glass composition in fly ash using quantitative X-ray diffraction. *Fuel* 85, 2268–2277. <https://doi.org/10.1016/j.fuel.2005.12.026>.
- Wen, C., Geng, L., Han, L., Wang, J., Chang, L., Feng, G., Kong, D., Liu, J., 2015. A comparative first principles study on trivalent ion incorporated SSZ-13 zeolites. *Phys. Chem. Chem. Phys.* 17, 29586–29596. <https://doi.org/10.1039/c5cp04788a>.
- Widiastuti, N., Hidayah, M.Z.N., Praseytoko, D., Fansuri, H., 2014. Synthesis of zeolite X-carbon from coal bottom ash for hydrogen storage material. *Adv. Mater. Lett.* 5, 453–458. <https://doi.org/10.5185/amlett.2014.amwec1019>.
- Winburn, R.S., Grier, D.G., McCarthy, G.J., Peterson, R.B., 2000. Rietveld quantitative X-ray diffraction analysis of NIST fly ash standard reference materials. *Powder Diffr.* 15, 163–172. <https://doi.org/10.1017/S0885715600011015>.
- Włodarski, M., Putkonen, M., Norek, M., 2020. Infrared absorption study of Zn-S hybrid and ZnS ultrathin films deposited on porous AAO ceramic support. *Coatings* 10, 459. <https://doi.org/10.3390/COATINGS10050459>.
- Wu, Z., Ahn, I.S., Lee, C.H., Kim, J.H., Shul, Y.G., Lee, K., 2004. Enhancing the organic dye adsorption on porous xerogels. *Colloids Surf. A Physicochem. Eng. Asp.* 240, 157–164. <https://doi.org/10.1016/j.colsurfa.2004.04.045>.
- Yang, L., Hu, J., He, L., Tang, J., Zhou, Y., Li, J., Ding, K., 2017. One-pot synthesis of multifunctional magnetic N-doped graphene composite for SERS detection, adsorption separation and photocatalytic degradation of Rhodamine 6G. *Chem. Eng. J.* 327, 694–704. <https://doi.org/10.1016/j.cej.2017.06.162>.
- Ye, Y., Shen, F., Wang, H., Chen, R., 2017. SSZ-13-supported manganese oxide catalysts for low temperature selective catalytic reduction of NO<sub>x</sub> by NH<sub>3</sub>. *J. Chem. Sci.* 129, 765–774. <https://doi.org/10.1007/s12039-017-1299-x>.
- Yin, Y., Yin, H., Wu, Z., Qi, C., Tian, H., Zhang, W., Hu, Z., Feng, L., 2019. Characterization of coals and coal ashes with high Si content using combined second-derivative infrared spectroscopy and Raman spectroscopy. *Crystals* 9, 1–12. <https://doi.org/10.3390/cryst9100513>.

Zhou, C., Liu, G., Xu, Z., Sun, H., Sing Lam, P.Kwan, 2018. Retention mechanisms of ash compositions on toxic elements (Sb, Se and Pb) during fluidized bed combustion. *Fuel* 213, 98–105. <https://doi.org/10.1016/j.fuel.2017.10.111>.

Zhou, Y., Min, Y., Qiao, H., Huang, Q., Wang, E., Ma, T., 2015. Improved removal of malachite green from aqueous solution using chemically modified cellulose by

anhydride. *Int. J. Biol. Macromol.* 74, 271–277. <https://doi.org/10.1016/j.ijbiomac.2014.12.020>.

Zones, S.L., 1985. Zeolite SSZ-13 and Its Method of Preparation U S Pat. 4, pp. 544–538 (<https://patents.google.com/patent/US4544538A/en>).